

RESEARCH ARTICLE

10.1002/2016WR019181

Transient forcing effects on mixing of two fluids for a stable stratification

María Pool^{1,2,3}, Marco Dentz^{1,2}, and Vincent E. A. Post³

¹Spanish National Research Council (IDAEA-CSIC), Barcelona, Spain, ²Associated Unit: Hydrogeology group (UPC-CSIC), Barcelona, Spain, ³School of the Environment, Flinders University, Adelaide, Australia

Key Points:

- We study effective mixing in temporally fluctuating one-dimensional flow for a stable stratification of two fluids of different density
- We derive a time-averaged model and explicit expressions for the concentration distribution and the variance
- The proposed formulation is found to provide very good predictions and correctly reproduces the numerical and experimental results

Correspondence to:

M. Pool,
mpoolr@gmail.com

Citation:

Pool, M., M. Dentz, and V. E. A. Post (2016), Transient forcing effects on mixing of two fluids for a stable stratification, *Water Resour. Res.*, 52, 7178–7197, doi:10.1002/2016WR019181.

Received 8 MAY 2016

Accepted 27 AUG 2016

Accepted article online 2 SEP 2016

Published online 22 SEP 2016

Abstract Mixing and dispersion in coastal aquifers are strongly influenced by periodic temporal flow fluctuations on multiple time scales ranging from days (tides), seasons (pumping and recharge) to glacial cycles (regression and transgressions). Transient forcing effects lead to a complex space and time-dependent flow response which induces enhanced spreading and mixing of dissolved substances. We study effective mixing and solute transport in temporally fluctuating one-dimensional flow for a stable stratification of two fluids of different density using detailed numerical simulation as well as accurate column experiments. We quantify the observed transport behaviors and interface evolution by a time-averaged model that is obtained from a two-scale expansion of the full transport problem, and derive explicit expressions for the center of mass and width of the mixing zone between the two fluids. We find that the magnitude of transient-driven mixing is mainly controlled by the hydraulic diffusivity, the period, and the initial interface location. At an initial time regime, mixing can be characterized by an effective dispersion coefficient and both the interface position and width evolve linearly in time. At larger times, the spatial variability of the flow velocity leads to a deceleration of the interface and a compression of its width, which is manifested by a subdiffusive evolution of its width as $t^{1/2}$.

1. Introduction

The study and proper quantification of solute mixing and spreading mechanisms in aquifers is the central importance not only for the design of water resources management and environmental remediation strategies, but also for the diagnosis and prediction of chemical reactions that result from mixing. Fluid mixing results from the fundamental competition between local deformation of the flow field and diffusion-dispersion mechanisms. Spatially nonuniform variations of the flow field are mainly controlled by the spatial variability of hydraulic properties of the subsurface (heterogeneity). The impact of heterogeneity on mixing and the induced non-Fickian behavior of solute transport have been examined extensively for the last four decades [see, e.g., *Kitanidis*, 1988; *Rajaram and Gelhar*, 1993; *Attinger et al.*, 1999; *Dentz et al.*, 2000]. Multi-scale heterogeneity leads to complex groundwater flow patterns with the existence of preferential flow paths which promote the creation of concentration gradients which in turn enhanced spreading and mixing of a dissolved substance.

In addition to heterogeneity of the medium, the temporal variability of the flow field due to transient effects may impact significantly on solute transport. Real systems are strongly influenced by periodic temporal flow fluctuations on multiple time scales in response to, for example, diurnal variations in evapotranspiration, tidal forcing, seasonal variations in recharge and pumping, as well as regressions and transgressions. Thus, aquifers are usually under perpetual nonequilibrium flow and solute transport conditions. Intensive research efforts over the last decades have been devoted to study the effects of temporal flow fluctuations on solute transport. It has been found that for heterogeneous porous media parallel fluctuations to the main flow direction have a limited impact on mixing, whereas transverse fluctuations to the main flow direction slightly enhance transverse dispersion and reduce longitudinal dispersion [see, e.g., *Rehfeldt and Gelhar*, 1992; *Dagan et al.*, 1996; *Dentz and Carrera*, 2003; *Cirpka and Attinger*, 2003; *de Dreuzy et al.*, 2012]. For homogeneous porous media with constant dispersion, *Dentz and Carrera* [2003] demonstrated that temporal flow fluctuations parallel to the main flow direction has little influence on mixing. However, for homogeneous porous media with velocity-dependent dispersion, *Kinzelbach and Ackerer* [1986], who derived an equivalent

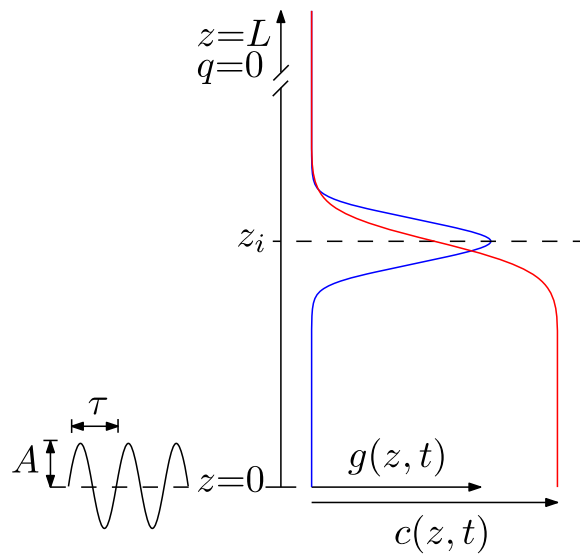


Figure 1. Schematic overview of the 1-D problem considered. A simple harmonic oscillation with an amplitude of $A [L]$ and a period of $\tau [T]$ is imposed at $z = 0$. The red line represents the vertical profile of the salt mass fraction distribution, $c(z, t)$, and the blue line represents its gradient, $g(z, t)$, which is maximum at the interface location z_i .

time-averaged coefficient to quantify the effect of temporal fluctuations on dispersion, found that transient forcing leads to an important increase in transverse dispersion whereas longitudinal dispersion is reduced. While all these investigations provide valuable insights into the effects of temporal fluctuations on mixing, aforementioned studies assumed stationarity of the flow field, i.e., an aquifer storativity of zero, which implies a uniform and instantaneous flow response to a hydraulic perturbation. With nonzero storativity, periodic forcing leads to a space and time-dependent flow response in which the oscillation amplitude is attenuated and decays exponentially with distance from the boundary whereas the phase lag increases linearly [see, e.g., *Jacob, 1950; Van Der Kamp, 1972; Townley, 1995*]. The resulting spatially nonuniform flow response may impact on the transient-induced mixing dynamics. In fact, *Goode and Konikow [1990]* showed that the effect of temporal fluctua-

tions on dispersion is controlled by a characteristic response time which depends on the aquifer hydraulic conductivity, the storativity, and the period. So far, it is not clear how the coupling of the aquifer storativity and transient forcing impact on solute transport.

In this paper, we study dispersion in nonstationary flow under different transient boundary conditions in order to identify and quantify the controls of the coupling between mixing and oscillatory transient flow. To this end, we study effective mixing in temporally fluctuating one-dimensional flow for a stable stratification of two fluids of different density. We derive an effective model and explicit expressions for the concentration distribution and the variance to capture and predict the mixing behavior. Numerical results and sand column experiments under well-controlled laboratory conditions are presented to validate the theoretical effective model defined.

2. Concepts and Methods

2.1. Problem Statement

We investigate solute mixing dynamics between two fluids of different density for a stable stratification under temporally fluctuating flow conditions. A one-dimensional system is considered with the z axis pointing vertically upward. Temporal flow fluctuations at $z = 0$ are characterized by a single harmonic with $A [L]$ being the oscillation amplitude and $\tau [T]$ the period. A sharp interface between the two fluids initially located at a distance of z_i from the boundary is considered. Mixing induced by transient-forcing effects is characterized by the increase in the width of the mixing zone which is quantified from the gradient $g(z, t)$ of the salt mass fraction distribution $c(z, t)$. Figure 1 depicts a schematic illustration of the problem considered.

2.2. Governing Equations

In the following, we state the flow and transport problems in terms of their governing equations and initial and boundary conditions, as well as available analytical expressions for the solution of the flow problem.

2.2.1. Flow

Momentum conservation in flow through porous media is expressed by Darcy's law, which considering small changes of density and saturated flow reads as

$$\mathbf{q}(\mathbf{x}, t) = -k \nabla h(\mathbf{x}, t), \quad (1)$$

where $\mathbf{q}(\mathbf{x}, t) [LT^{-1}]$ is fluid velocity, $k [LT^{-1}]$ hydraulic conductivity and $h(\mathbf{x}, t) [L]$ is the hydraulic head.

Fluid mass balance in the absence of sinks and sources is given by the continuity equation

$$\frac{\partial \phi \rho}{\partial t} = -\nabla \cdot \mathbf{q} \rho, \tag{2}$$

where ϕ [$L^3 L^{-3}$] is the porosity and ρ [ML^{-3}] fluid density. Assuming ρ to be constant and expanding the storage term, one can write [Bear, 1972]

$$S_s \frac{\partial h(\mathbf{x}, t)}{\partial t} = \nabla \cdot \mathbf{q}(\mathbf{x}, t), \tag{3}$$

where S_s [L^{-1}] denotes specific storativity defined as $S_s = \rho a_g [(1 - \phi)\beta_m + \phi\beta_w]$, in terms of a_g [LT^{-2}] the gravitational acceleration, β_w [$LT^2 M^{-1}$] the water compressibility, $4.47 \times 10^{-10} \text{ m s}^2 \text{ kg}^{-1}$ for pure water at 20°C, and β_m [$LT^2 M^{-1}$] the bulk porous matrix compressibility, which ranges from 10^{-10} for sound bedrock to about $10^{-7} \text{ m s}^2 \text{ kg}^{-1}$ for clay [Freeze and Cherry, 1979].

Equation (3) is subject to the following boundary conditions. The upper boundary is assumed to be located far from the interface between the two fluids ($z = L$, with $L \gg z_i$) where the response to the fluctuations is diminished so that the gradient of h can be considered to be zero (no-flow boundary of both salt and water). In order to examine the response of the flow field to the transient-forcing boundary, two different types of time-fluctuating boundary conditions are considered at $z = 0$. First, equation (3) is subject to a dynamic specified flux (Neumann-type boundary condition), which reads as

$$q_b(\mathbf{x}, t)|_{z=0} = q_r + \frac{Ak}{L} \sin \frac{2\pi t}{\tau}, \tag{4}$$

and second, equation (3) is subject to a periodic prescribed head (Dirichlet-type boundary condition), which is given by

$$h_b(\mathbf{x}, t)|_{z=0} = h_r + A \sin \frac{2\pi t}{\tau}, \tag{5}$$

where q_r [LT^{-1}] and h_r [L] represent a reference flux and head, respectively, considered here to be zero for simplicity.

These boundary conditions render the flow field one-dimensional, aligned with the z direction of the coordinate system. It is denoted by $q(z, t)$ in the following. The solutions for $q(z, t)$ for the specified boundary conditions, equations (4) and (5) can be written, respectively, in the compact way [see, e.g., Jacob, 1950; Ferris, 1951],

$$q(z, t) = q_0 \exp(-\mu z) \sin\left(\frac{2\pi t}{\tau} - \mu z + \varphi\right), \tag{6}$$

where $\mu = \sqrt{S_s \pi / k \tau}$ [L^{-1}] is a wave number which depends on the hydraulic diffusivity (with k/S_s , hydraulic conductivity, and specific storage, in confined aquifers or T/S , transmissivity and storage coefficient, in unconfined aquifers) and the period, and represents the inverse of a characteristic distance in response to periodic transient flow. For Neumann boundary conditions we define

$$q_0 = \frac{Ak}{L}, \quad \varphi = 0, \tag{7}$$

while for Dirichlet boundary conditions, we set

$$q_0 = \sqrt{2} Ak \mu, \quad \varphi = \frac{\pi}{4}. \tag{8}$$

Note that a spatially nonuniform flow field is obtained from both solutions when considering a finite storativity ($S_s \neq 0$). However, the solution for periodic transient forcing strongly depends on the boundary conditions [Townley, 1995]. Thus, for the case of $S_s = 0$ and considering a Neumann-type boundary condition, the time-dependent flow field is spatially uniform (instantaneous flow response to hydraulic perturbation), whereas $q = 0$ when imposing a Dirichlet-type boundary condition due to an instantaneous head response to hydraulic perturbation.

2.2.2. Transport

Solute mass conservation can be expressed in terms of the solute mass fraction $c(\mathbf{x}, t)$ [MM^{-1}] (mass of dissolved solute per unit mass of fluid), and is given by

$$\frac{\partial \phi \rho c}{\partial t} = -\nabla \cdot \mathbf{q} \rho c + \nabla \cdot \phi \rho \mathbf{D}_h \nabla c, \quad (9)$$

where $\mathbf{D}_h(\mathbf{x}, t)$ [L^2T^{-1}] is the hydrodynamic diffusion-dispersion tensor, defined as $\mathbf{D}_h(\mathbf{x}, t) = [\mathbf{D}(\mathbf{x}, t) + D_m \mathbf{I}]$ with D_m [L^2T^{-1}] the molecular diffusion coefficient, \mathbf{I} the identity matrix and $\mathbf{D}(\mathbf{x}, t)$ [L^2T^{-1}] the dispersion tensor defined in terms of α_L [L] and α_T [L], the longitudinal and transverse dispersivities, respectively [e.g., Bear, 1972].

Multiplication of (2) by c and subsequent subtraction from (9) gives the following transport equation for the solute mass fraction c :

$$\frac{\partial c(\mathbf{x}, t)}{\partial t} = -\mathbf{v}(\mathbf{x}, t) \cdot \nabla c(\mathbf{x}, t) + \nabla \cdot \mathbf{D}_h(\mathbf{x}, t) \nabla c(\mathbf{x}, t), \quad (10)$$

where $\mathbf{v}(\mathbf{x}, t)$ [LT^{-1}] denotes the pore water velocity, $\mathbf{v}(\mathbf{x}, t) = \mathbf{q}(\mathbf{x}, t) / \phi$.

The transport equation (10) is subject to natural boundary conditions at $z = \infty$ and a nondispersion boundary condition at $z = 0$. This implies that the salt mass fraction equals either that of the maximum (c_m) for fluid inflows or that of the resident mass fraction for fluid outflows [Voss and Souza, 1987; Frind, 1982]. The initial condition is given by a step input of $c = c_m$ for $z \leq z_i$ and 0 else.

The initial and boundary conditions for flow and transport render the transport problem one-dimensional,

$$\frac{\partial}{\partial t} c(z, t) = -v(z, t) \frac{\partial}{\partial z} c(z, t) + \frac{\partial}{\partial z} [D(z, t) + D_m] \frac{\partial}{\partial z} c(z, t), \quad (11)$$

where the dispersion coefficient is defined as $D(z, t) = \alpha_L |v(z, t)|$.

In order to study the mixing zone, which develops around the step position z_i , we consider the normalized gradient of the salt mass fraction distribution, which is given by

$$g(z, t) = -\frac{1}{c_m} \frac{\partial c(z, t)}{\partial z}. \quad (12)$$

Note that the integral of the derivative of $c(z, t)$ over the transport domain is simply equal to $-c_m$. Differentiation of (11) with respect to z gives the following governing equation for $g(z, t)$:

$$\frac{\partial}{\partial t} g(z, t) = -\frac{\partial}{\partial z} v(z, t) g(z, t) + \frac{\partial^2}{\partial z^2} [D(z, t) + D_m] g(z, t). \quad (13)$$

Note that this equation is mass conservative, unlike equation (11) for the salt mass fraction. Thus, the transport of $g(z, t)$ can be directly formulated in a particle-based framework. The Langevin equation equivalent to (13) is given by [Kinzelbach, 1988; Risken, 1996]

$$\frac{dz(t)}{dt} = v[z(t), t] + \sqrt{2[D[z(t), t] + D_m]} \zeta(t), \quad (14)$$

where we use the Ito interpretation of the stochastic integral and $\zeta(t)$ is a Gaussian white noise characterized by 0 mean and covariance

$$\langle \zeta(t) \zeta(t') \rangle = \delta(t - t'). \quad (15)$$

The angular brackets denote the average over all noise realizations. The initial position is given by $z(t=0) = z_i$. In the following, we make use of both the Eulerian and Lagrangian pictures of transport.

2.3. Dispersion and Mixing

The impact of periodic temporal fluctuations on dispersion and the width of the mixing zone is characterized by the second centered moment, or variance of the gradient $g(z, t)$ of the salt mass fraction $c(z, t)$ [Dentz and Carrera, 2003; Dentz et al., 2011a; Cirpka and Attinger, 2003], which is defined by

$$\sigma^2(t) = m_2(t) - m_1(t)^2. \tag{16}$$

The first and second moments $m_1(t)$ and $m_2(t)$ of $g(z, t)$ are given by

$$m_i(t) = \int_0^\infty dz z^i g_z(z, t) \tag{17}$$

for $i = 1, 2$.

In order to characterize the increase of the variance of the mixing zone, we define an apparent dispersion coefficient in terms of the average rate of change of $\sigma^2(t)$ as

$$D_h^a = \frac{\sigma^2(t)}{2t}. \tag{18}$$

Under uniform homogeneous flow conditions, the width of the mixing zone $\sigma(t)$ provides a measure for mixing; this means it characterizes the decay of the maximum concentration. For transport in space and time variable flow fields, this is in general not the case [Dentz et al., 2011b]. Under such conditions, the mixing zone between the invading and displaced fluids can be characterized by the dilution index $E(t)$, an entropy-based measure that quantifies the mixing volume [Kitanidis, 1994]. It is defined by

$$E(t) = \exp[-H(t)], \quad H(t) = \int_0^\infty dz g(z, t) \ln g(z, t), \tag{19}$$

where $H(t)$ is the entropy of the gradient distribution $g(z, t)$. The dilution index is a measure for the mixing state of a system.

3. Effective Transport

Here we systematically quantify the effect of temporal fluctuations on the evolution of the gradient $g(t)$ and the mass fraction $c(t)$. We are interested in the leading behavior for times $t \gg \tau$ that emerges as a result of temporal and spatial flow fluctuations. To this end, we consider the evolution of the time-average $g_0(z, t)$ of $g(z, t)$, which is defined by

$$g_0(z, t) = \frac{1}{\tau} \int_0^\tau dt' g(z, t+t'). \tag{20}$$

The first and second spatial moments of $g_0(z, t)$ are given by

$$m_i^e(t) = \int_0^\infty dz z^i g_0(z, t), \tag{21}$$

for $i = 1, 2$. The effective center of mass position is given by $m_1^e(t)$. The effective variance $\sigma_e^2(t)$ is defined by

$$\sigma_e^2(t) = m_2^e(t) - m_1^e(t)^2. \tag{22}$$

3.1. Effective Equation

In order to derive a governing equation for $g_0(z, t)$, we employ a two-scale expansion in a small parameter $\epsilon = \tau/T$ where T is a characteristic macroscopic observation time. In Appendix A, we derive the effective transport equation

$$\frac{\partial g_0(z, t)}{\partial t} + \frac{\partial}{\partial z} v_e(z) g_0(z, t) - \frac{\partial^2}{\partial z^2} [D_e(z) + D_m] g_0(z, t) = 0, \tag{23}$$

which describes the transport behavior for $t \gg \tau$. The effective velocity $v_e(z)$ and dispersion coefficient $D_e(z)$ are given by

$$v_e(z) = \frac{v_0^2 \mu \tau \exp(-2\mu z)}{4\pi}, \quad D_e(z) = \frac{2\alpha_L v_0}{\pi} \exp(-\mu z), \quad (24)$$

where $v_0 = q_0 / \phi$ with q_0 defined in (7) and (8) for Neumann and Dirichlet boundary conditions, respectively. From (23), we obtain by integration in z the effective equation for the average solute mass fraction c_0

$$\frac{\partial c_0(z, t)}{\partial t} + v_e(z) \frac{\partial}{\partial z} c_0(z, t) - \frac{\partial}{\partial z} [D_e(z) + D_m] \frac{\partial}{\partial z} c_0(z, t) = 0. \quad (25)$$

The average transport equation (23) is equivalent to the Langevin equation

$$\frac{dz(t)}{dt} = v_e[z(t)] + \sqrt{2(D_e[z(t)] + D_m)} \xi(t), \quad (26)$$

where we use the Ito interpretation of the stochastic integral. The mass fraction gradient $g_0(z, t)$ is given in terms of the particle trajectories $z(t)$ by $g_0(z, t) = \langle \delta[z - z(t)] \rangle$. The moments (21) of $g_0(z, t)$ then are given by

$$m_i^g(t) = \langle z(t)^i \rangle. \quad (27)$$

Numerical solutions for the effective variance $\sigma_e^2(t)$ and center of mass position $m_1^g(t)$ are based on the discretized version of (26), which is given by

$$z(t + \Delta t) = z(t) + v_e[z(t)]\Delta t + \sqrt{2(D_e[z(t)] + D_m)\Delta t} \eta(t), \quad (28)$$

where the $\eta(t)$ are Gaussian random numbers with 0 mean and unit variance.

3.2. Approximate Solution

Here we derive approximate solutions for the effective gradient of the solute mass fraction $g_0(z, t)$ and the mass fraction $c_0(z, t)$, as well as the effective center of mass position $m_1^g(t)$ and variance $\sigma_e^2(t)$. To this end, we expand $z(t)$ about the purely advective solution $z_0(t)$, which solves (26) for $\xi(t) \equiv 0$. Thus, $z_0(t)$ satisfies the advection equation

$$\frac{dz_0(t)}{dt} = v_e[z_0(t)]. \quad (29)$$

Inserting the explicit expression (24), the latter can be integrated by separation of variables, which gives

$$z_0(t) = z_i + \frac{1}{2\mu} \ln(t/\tau_v + 1), \quad (30)$$

where we defined the characteristic time scale

$$\tau_v = \frac{2\pi \exp(2\mu z_i)}{v_0^2 \mu^2 \tau}. \quad (31)$$

It measures the characteristic advection time over the distance $2/\mu$ by the initial velocity $v_e(z_i)$. For $t \ll \tau_v$, the interface position $z_0(t) = z_i + t/(2\mu\tau_v) = z_i + v_e(z_i)t$. The time scale τ_v sets the time at which the interface starts decelerating, which, as we will see in the following, leads to a compression of the interface and thus a slowing down of the growth of the interface width.

We consider now the shifted variable $z'(t) = z(t) - z_0(t)$. Note that the effective mean and variance are given in terms of $z'(t)$ as

$$m_1^g(t) = \langle z'(t) \rangle + z_0(t), \quad \sigma_e^2(t) = \langle z'(t)^2 \rangle - \langle z'(t) \rangle^2. \quad (32)$$

Furthermore, $g_0(z, t)$ is given in terms of the distribution $g'_0(z', t)$ of z' as

$$g_0(z, t) = g'_0[z - z_0(t), t]. \quad (33)$$

Inserting $z'(t) = z(t) - z_0(t)$ into (26) and using (29) yields

$$\frac{dz'(t)}{dt} = (v_e[z'(t) + z_0(t)] - v_e[z_0(t)]) + \sqrt{2(D_e[z'(t) + z_0(t)] + D_m)} \xi(t), \quad (34)$$

with the initial condition $z'(t=0) = 0$. For $\langle z'(t) \rangle \ll 1$, we can expand (34) as

$$\frac{dz'(t)}{dt} = -\gamma(t)z'(t) + \sqrt{2[\mathcal{D}(t) + D_m]}\zeta(t), \tag{35}$$

where we defined

$$\gamma(t) = -\frac{dv_e[z_0(t)]}{dz}, \quad \mathcal{D}(t) = D_e[z_0(t)]. \tag{36}$$

Equation (35) describes a non-stationary Ornstein-Uhlenbeck process [Risken, 1996]. Note that the linear approximation (35) is only valid as long as $\sigma_e^2(t) \ll z_0(t)^2$. The latter sets the time scale τ_a for which the approximation is valid as $\sigma_e^2(\tau_a) = z_0(\tau_a)^2$. Note also that $\gamma(t) > 0$ because the effective flow velocity decreases with increasing z . This implies that the dispersive interface experiences compression due to the spatial deceleration of the flow velocity as well as expansion due to dispersion and diffusion, as expressed by (35) [Le Borgne et al., 2013; Dentz and de Barros, 2015].

3.2.1. Effective Center of Mass Position and Variance

In order to solve for the effective center of mass position and variance, we derive their governing equations from (35).

By averaging (35) over the noise, we obtain

$$\frac{d\langle z'(t) \rangle}{dt} = -\gamma(t)\langle z'(t) \rangle. \tag{37}$$

For the initial condition $z'(t=0)=0$, we obtain $\langle z'(t) \rangle = 0$. This implies that the effective center of mass position can be approximated by

$$m_1^e(t) = z_0(t). \tag{38}$$

For $t \ll \tau_v$ the center of mass migrates linearly with time as $v_e(z)t$, with $v_e(z)$ defined in (24). At increasing times $t \gg \tau_v$, the interface is wide enough to experience the spatial variability of the velocity field induced by the storativity, which leads to a compression of the mixing zone. As a result, the interface decelerates leading to a logarithmic upward displacement of the center of mass (see equation (30)).

Similarly, we obtain an equation for the variance $\sigma_e^2(t)$ by multiplying (35) with $z'(t)$, using the Ito formula [Risken, 1996] and subsequent averaging. This gives

$$\frac{d\sigma_e^2(t)}{dt} = -2\gamma(t)\sigma_e^2(t) + 2[\mathcal{D}(t) + D_m]. \tag{39}$$

This equation quantifies the competition between interface compression represented by the compression rate $\gamma(t)$ and hydrodynamic dispersion and diffusion given by the time-dependent $\mathcal{D}(t)$ and the constant D_m , respectively. Unlike in purely diffusive mixing problems [Le Borgne et al., 2013; Dentz and de Barros, 2015], here the flow velocity impacts on the dynamics of the width of the mixing zone through the compression as well as the dispersion term. Equation (39) can be integrated by separation of variables, which gives

$$\sigma_e^2(t) = \sigma^2(0)\exp[-2\Gamma(t)] + 2\exp[-2\Gamma(t)] \int_0^t dt' [\mathcal{D}(t') + D_m] \exp[2\Gamma(t')], \tag{40}$$

where $\sigma^2(0)$ is the initial variance of the mixing zone and

$$\Gamma(t) = \int_0^t dt' \gamma(t'). \tag{41}$$

Appendix B derives the following explicit expression for the effective variance:

$$\sigma_e^2(t) = \frac{\sigma^2(0)}{(1+t/\tau_v)^2} + \frac{4D_e\tau_v}{5} \left[\frac{(1+t/\tau_v)^{5/2} - 1}{(1+t/\tau_v)^2} \right] + 2D_mt \left[\frac{1}{3} + \frac{(1+t/\tau_v)^2 - 1}{3t/\tau_v(1+t/\tau_v)^2} \right], \tag{42}$$

where we defined

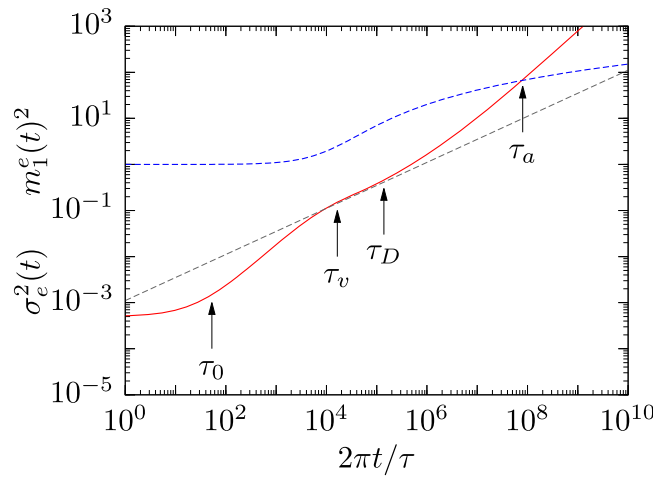


Figure 2. Illustration of the effective variance $\sigma_e^2(t)$ (solid red line) given by (42) and center of mass position $m_1^e(t)$ (dashed blue line) given by (30) for $\tau_v = 10^7$ s, $\mu = 1/2$ m⁻¹, $D_e = 10^{-7}$ m²/s, $D_m = 10^{-9}$ m²/s, $\sigma^2(0) = 10^{-3}$ m², and $z_i = 1$ m. The arrows denote, from left to right, the diffusion time scale $\tau_0 = \sigma^2(0)/(D_e^e + D_m)$ over the initial mixing zone, the time scale τ_v given by (31), which marks the breakdown of the linear dispersion regime, the time scale τ_D given by (45) and the time scale τ_a at which $\sigma_e^2(\tau_a) = z_0(\tau_a)^2$, which sets the limit of validity of the approximation (42) for $\sigma_e^2(t)$. The thin dashed gray line indicates the subdiffusive $t^{1/2}$ -behavior for $\tau_v \ll t \ll \tau_D$.

$$D_e = \frac{2}{\pi} \alpha_L v_0 \exp(-\mu z_i). \quad (43)$$

Different regimes in the temporal evolution of the variance are identified. Figure 2 shows the evolution of $\sigma_e^2(t)$ and the behaviors in the different time regimes. For times $\tau_0 \ll t \ll \tau_v$, with τ_0 the dispersion time over the initial width of the mixing zone given by $\tau_0 = \sigma^2(0)/(D_e + D_m)$ and τ_v the characteristic time defined in (31), the interface is mainly influenced by the velocities around the interface location (z_i), where the gradient is maximum. Thus, the mixing zone grows linearly with time and $\sigma_e^2(t) = 2D_h^e t$ with the effective dispersion coefficient

$$D_h^e = D_e + D_m. \quad (44)$$

In this time regime, the apparent dispersion coefficient D_h^a defined by (18) is $D_h^a = D_h^e$. Note that under steady state conditions ($\mu = 0$) and for $D_m = 0$

expression (44) reduces to the expression for the longitudinal dispersion coefficient derived by Kinzelbach and Ackerer [1986].

For $t \gg \tau_v$, the interface starts sampling the strong velocity contrast induced by the exponential decay in amplitude with distance from the boundary, which implies the deceleration of the center of mass. Therefore, τ_v marks the time scale after which the interface starts to decelerate, which leads to a compression of the interface.

The time scale

$$\tau_D = \frac{4 D_e^2}{25 D_m^2} \tau_v \quad (45)$$

sets the time after which the diffusive second term in (42) wins over the dispersive first terms. If $\tau_v \ll \tau_D$, we observe an intermediate time regime for which the variance increases subdiffusively as $\sigma_e^2(t) \propto t^{1/2}$ due to interface compression. For times larger than τ_D and smaller than τ_a the variance increases diffusively as $\sigma_e^2(t) = 2D_m t/3$. The time scale τ_a marks the validity limit of the approximation (35), after which $\sigma_e(t) > m_1^e(t)$.

3.2.2. Gradient Distribution and Dilution Index

The Fokker-Planck equation for $g'_0(z', t)$ corresponding to the Langevin equation (35) is

$$\frac{\partial g'_0(z', t)}{\partial t} = - \frac{\partial}{\partial z'} \gamma(t) z' g'_0(z', t) + \frac{\partial}{\partial z'} [D(t) + D_m] \frac{\partial}{\partial z'} g'_0(z', t). \quad (46)$$

Its solution is given by a Gaussian characterized by the mean $\langle z' \rangle$ and the variance $\sigma_e^2(t)$. Thus, we obtain for $g_0(z, t)$ according to (33)

$$g_0(z, t) = \frac{\exp\left(-\frac{[z - z_0(t)]^2}{2\sigma_e^2(t)}\right)}{\sqrt{2\pi\sigma_e^2(t)}}. \quad (47)$$

According to (12), we then obtain by integration for the effective solute mass fraction

$$c_0(z, t) = \frac{c_m}{2} \operatorname{erfc}\left[\frac{z - z_0(t)}{\sqrt{2\sigma_e^2(t)}}\right]. \quad (48)$$

We obtain from (47) for the dilution index (19) the expression

$$E(t) = \sqrt{2\pi e \sigma_e^2(t)}. \tag{49}$$

In the early time regime ($t < \tau_v$), characterized by a linear increase of the variance, the dilution index increases as $E(t) \propto t^{1/2}$. However, in the late time regime ($t > \tau_v$), the dilution index enhances subdiffusively as $E(t) \propto t^{1/4}$ due to compression of the interface induced by the impact of the exponential decay in flow velocities.

Solute mixing and thus dilution is quantified fully in terms of the effective width of mixing zone $\sigma_e^2(t)$. Note that $\sigma_e^2(t)$ is derived from the time averaged gradient distribution (47). In the following, we will compare these results to direct numerical simulations of the full flow and transport problem.

4. Numerical Investigation

In this section, we present a detailed numerical investigation of the full flow and transport problem posed in section 2.2. We first describe the numerical methodology, and then discuss the results for the apparent dispersion, variance of the gradient distribution and dilution index.

4.1. Methodology

Several sets of simulations were carried out to evaluate the impact of transient-forcing flow on mixing and to test accuracy of the proposed effective model. One-dimensional numerical simulations were performed with the code TRANSIN [Medina and Carrera, 2003], which solves the flow and transport equations using linear finite elements for spatial discretization and weighted finite differences for time integration [see, e.g., Vázquez-Suñé et al., 2005; Abarca et al., 2006]. In order to better assess the effects of the spatial variability of the flow field on the transient-driven mixing dynamics, runs were performed by independently varying the storage coefficient (S) and the interface location (z_i). The spatial and temporal discretization were defined to ensure accuracy and numerical stability. Table 1 summarizes the parameters used for all numerical simulations.

4.2. Results

4.2.1. Apparent Dispersion

We focus first on the transient-induced linear growth of the variance for $t \ll \tau_v$. Figure 3 shows the comparison between numerical results for the apparent dispersion coefficient computed from the first and second moments of the gradient of the concentration distribution given by (18) with the analytical prediction (44). Numerical and predicted results are displayed with respect to the storage coefficient and the interface location normalized by the maximum extent of the response to the temporal fluctuations ($z_i = 4.5/\mu$), defined as the characteristic distance at which the response to the temporal fluctuations becomes less than 1%. Results obtained from the analytical solution derived by Kinzelbach and Ackerer [1986] using a Neumann-type boundary condition and results for the purely diffusive case are also included for illustration. Note that for all cases the predictions of the effective model are in good agreement with the numerical results.

For the case of transient Neumann-type boundary conditions (Figures 3a and 3b), D_h^a is maximum if the storativity is small and the interface is close to the boundary. This is due to the spatial dependence of the velocity field, which is controlled by the factor $e^{-z\mu}$ (equation (6), with q_0 defined in (7)). Thus, an increase in the storativity, and then in the wave number μ , or in the distance of the interface from the boundary, tends to favor the exponential decay of the velocity and, as a result, D_h^a coefficient decreases. Similar results were

obtained by Goode and Konikow [1990] who found that the maximum impact of temporal fluctuations on mixing occurs for quasi steady flow conditions ($S = 0$).

Note that the scaling of z_i with the maximum distance of influence of the fluctuating boundary condition (z_i) allows us to collapse the predicted and numerical data onto a single curve for the case of using a Neumann-type

Table 1. Parameters Used in Numerical Simulations

Parameter	Value	Description
L (m)	52	Domain length
T ($m^2 s^{-1}$)	1.23e-4	Transmissivity
S	0-0.1	Storage coefficient
ϕ	0.25	Porosity
α_L (m)	1e-3	Longitudinal dispersivity
D_m ($m^2 s^{-1}$)	1e-9	Molecular diffusion coefficient
A (m)	0.05	Oscillation amplitude
τ (s)	7200	Oscillation period
z_i (m)	0.5-4	Interface location

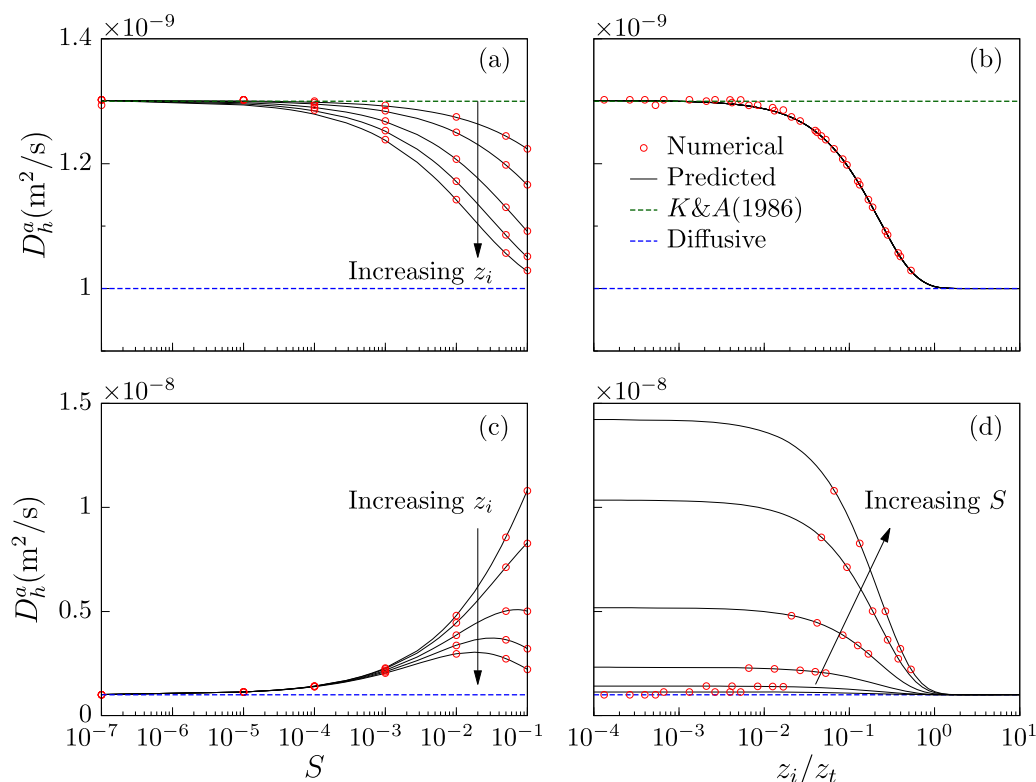


Figure 3. Apparent dispersion coefficient as a function of (a, c) the storativity (S) for (top to bottom) $z_i = 0.5, 1, 2, 3,$ and 4 m; and (b, d) the interface location (z_i) normalized by the maximum extent of the hydraulic influence of the temporal fluctuations ($z_i = 4.5/\mu$) for (bottom to top) $S = 0, 1e-5, 1e-4, 1e-3, 1e-2, 5e-2, 1e-1$, with (a, b) a Neumann-type boundary condition and (c, d) a Dirichlet-type boundary condition. Black solid lines represent predictions from the equation (44), red dots represent the numerical results, dark-green dashed lines represent the results obtained from the analytical solution of Kinzelbach and Ackerer [1986] and blue dashed lines represent the results for a purely diffusive problem.

boundary condition (Figure 3b). In this case, it can be observed that the apparent dispersion coefficient evolves with increasing μ and z_i from the solution obtained for the quasi steady state problem [Kinzelbach and Ackerer, 1986] to the one purely diffusive for a distance of the interface from the boundary of $z_i \geq z_i$. Therefore, numerical and analytical results provide evidence that no transient-driven mixing occurs and the enhancement of the interface becomes purely diffusive for $z_i \geq 4.5/\mu$.

A similar effect of the interface location on mixing is observed when considering a Dirichlet-type boundary condition (see Figure 3d), with a maximum impact for small distances of the interface from the boundary. This is consistent with Chen and Pinder [2011a, 2011b], who numerically and experimentally demonstrated that the further the interface is from the boundary, the smaller the impact of the temporal fluctuating boundary conditions on dispersion. However, in this case, an increase in the storativity causes the transient-induced mixing to increase (see Figure 3c). This is because an increase in the storativity, although implying an increase in μ so that the extent of the aquifer response to the fluctuations is reduced, leads to a more nonuniform hydraulic response to the temporal fluctuations with higher flow velocities (equation (6), with q_0 defined in (8)). Thus, the resulting delayed flow response to the temporal fluctuations increases the velocity variability, which in turn leads to an increase in the apparent dispersion coefficient.

4.2.2. Variance and Center of Mass Position

The comparison of predicted and numerical results of the temporal evolution the variance for different values of the storativity is shown in Figure 4. As previously discussed, when considering a Neumann-type boundary condition transient-driven mixing evolves from the quasi-steady state solution to purely diffusive mixing with increasing distance of the interface from the boundary, and the transition is faster as the storativity increases. On the other hand, for Dirichlet-type boundary conditions, temporal fluctuations have the largest impact on mixing as the storativity increases. Note that for all the cases and considering the same fluctuation amplitude and period, the variance and thus, for $t \ll \tau_v$, the apparent dispersion coefficient are larger for a Dirichlet-type boundary condition than for Neumann-type boundary condition. Thus, for the

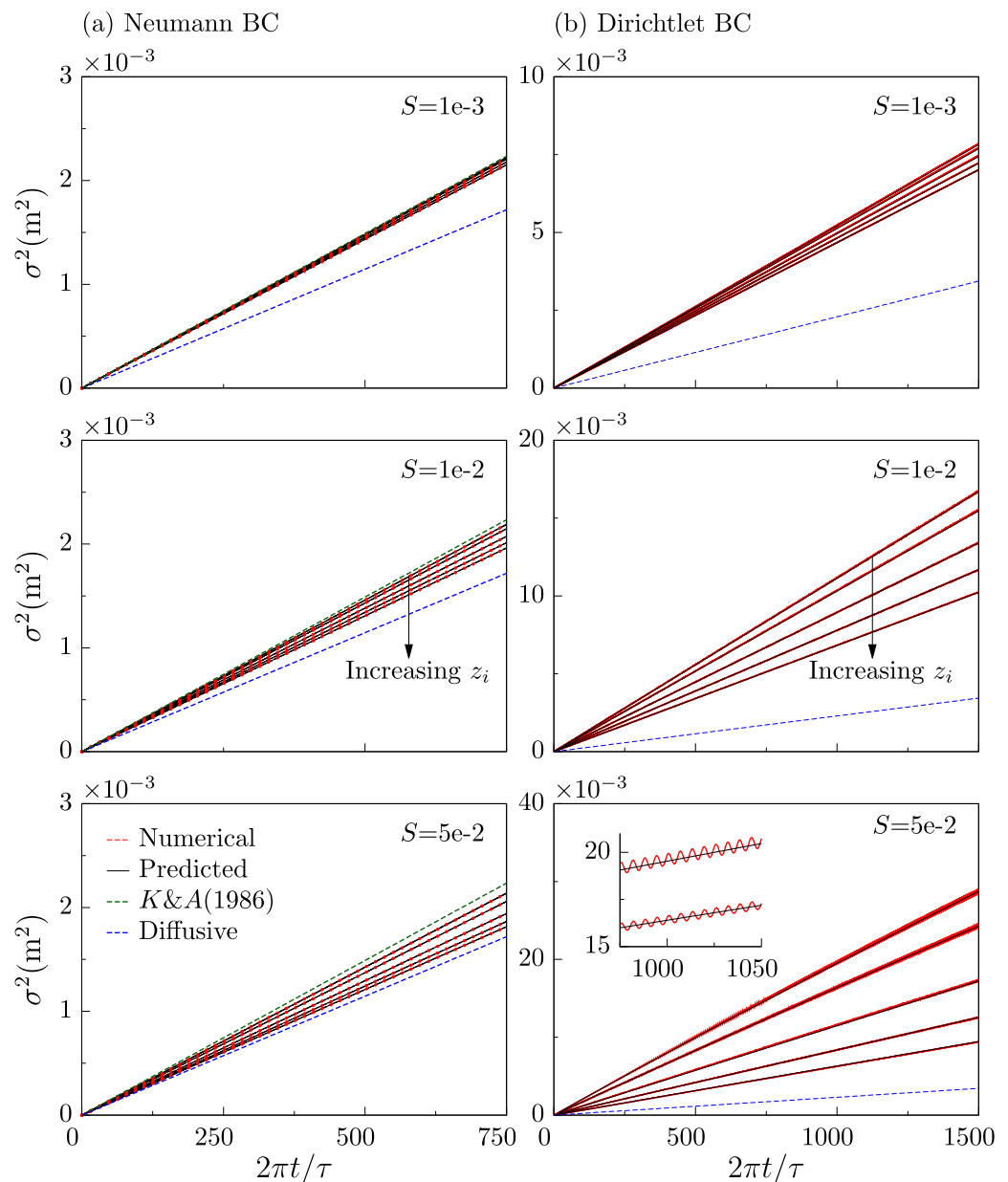


Figure 4. Temporal behavior of the variance of the gradient of concentration for different interface locations, showing the effect of varying the storage coefficient S . Black solid lines represent predictions from the effective model, red dots and lines represent the numerical results with Neumann and Dirichlet boundary conditions, respectively, dark green dashed lines represent the results obtained from the analytical solution of Kinzelbach and Ackerer [1986] and blue dashed lines represent the results for a purely diffusive problem.

case with $S = 5e-2$, the variance is over 1 order of magnitude larger for Dirichlet than Neumann-type boundary condition.

Note also that fluctuations about the mean variance are observed when considering a Dirichlet-type boundary condition, especially for large storativity values (see inset in Figure 4b). This behavior is due to the effect of the stretching and compression of the interface induced by the delayed response in the velocity field. Thus, when the head fluctuation at the boundary is reaching its highest level, the upward migration of the mixing zone is faster at the lower part of the interface compared to the one at the upper part, leading to a local compression of the interface. This effect causes the width of the mixing zone to decrease. In contrast, when the head at the boundary falls from the mean level to the lowest level, the faster downward migration of the saline end of the interface induces stretching of the interface which leads to an increase in the width of the mixing zone. The analytical solution (42) for the effective variance accurately predicts the average increase of the variance.

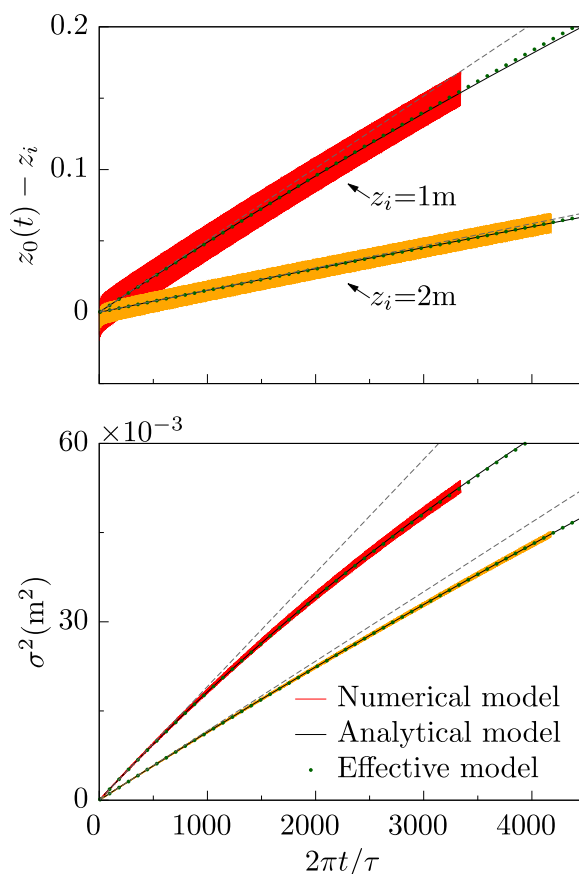


Figure 5. Temporal behavior of the center of mass and variance for a storativity of $S = 1e-1$ and different interface locations. Red and orange lines represent numerical results for $z_i = 1$ m and $z_i = 2$ m, respectively, black solid lines represent predictions from the equation (42) and gray dashed lines represent results for the linear regime.

As pointed out above, the growth of the variance is essentially linear for $t \ll \tau_v$ and characterized by the effective dispersion coefficient (44). In this time regime the center of mass of the gradient distribution increases linearly as discussed in section 3.2. For $t \gg \tau_v$, however, the interface decelerates, which leads to a compression of the mixing zone. These mechanisms are manifest in a sublinear behavior as $\sigma^2 \propto t^{1/2}$. The time scale τ_v given by (31) depends critically on the spatial variability of the velocity field. It is therefore controlled by the oscillation amplitude, the wave number, the period and the interface location. The smaller the storativity and the amplitude, and the longer the period, the more uniform the velocity field, and then the longer it takes to arrive at the subdiffusion regime.

The numerical results and the predictions of (30) and (42) for the center of mass position of the gradient distribution and variance for $S = 1e-1$ and Dirichlet-type boundary conditions are shown in Figure 5. The effective model accurately captures the linear and nonlinear behaviors of the center of mass position and variance.

4.2.3. Solute Mass Fraction, Gradient Distribution, and Dilution Index

Profiles of the solute mass fraction and gradient distribution for different storativity values are shown in Figure 6. The analytical solutions (48) and (47) predict the numerical results accurately, which confirms the validity of the approximation in section 3.2 not only for the

center of mass position and variance but also for the full concentration profiles. For increasing time, however, when the gradient distribution is wide enough to notice the nonlinear nature of the velocity profile, the distribution becomes asymmetric. Note that the approximation in section 3.2 relies on a linearization of the flow velocity about the purely advective interface position. The tendency toward asymmetry at longer times characterized by a larger degree of mixing at the saline end of the interface where the velocities are higher can be observed in Figure 7. Similar asymmetry in the freshwater-seawater interface has been reported in field studies of tidally dominated coastal aquifers where vertical salinity profiles are usually characterized by a steeper gradient at the freshwater end of the mixing zone [see, e.g., Stoessell, 1995; Oki et al., 1998; Bonnesen et al., 2009].

Figure 8 shows the evolution of the dilution index obtained from the direct numerical simulations and the analytical prediction (49), which relies on the time-average gradient distribution. The analytical results predict the numerical behavior accurately which indicates that solute mixing is well represented by the effective variance (42). The dilution index increases first as $E(t) \propto t^{1/2}$, which reflects the linear growth of the variance of the mixing zone for $t \ll \tau_v$. At increasing times $t \gg \tau_v$, the spatial deceleration and subsequent compression leads to the observed subdiffusive growth of the dilution index as $E(t) \propto t^{1/4}$.

5. Sand Column Experiments

Transient forcing experiments were performed on a uniformly packed sand column under well-controlled laboratory conditions in order to investigate the mixing dynamics of two fluids of different density for a stable stratification under temporally fluctuating flow conditions.

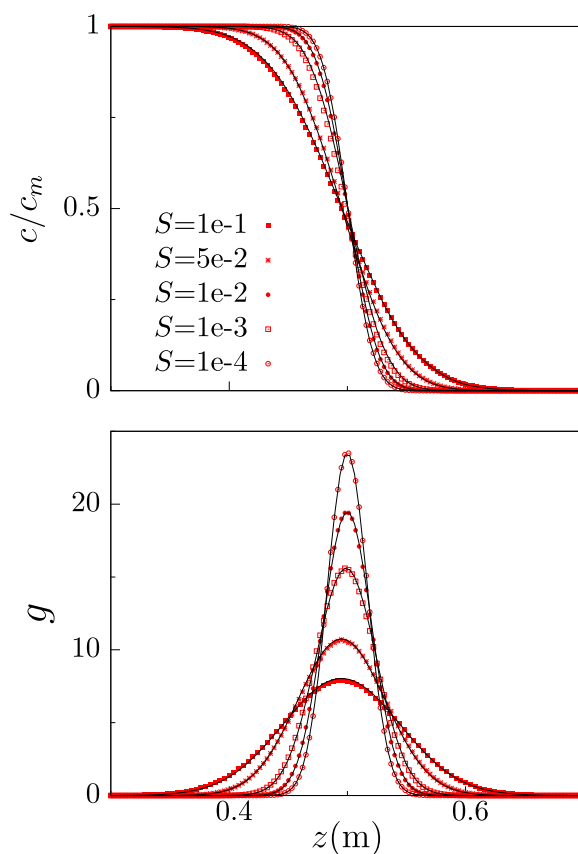


Figure 6. Impact of the storativity on the concentration and gradient distributions under periodic transient forcing considering a Dirichlet-type boundary condition at a specific time ($2\pi t/\tau = 1500$) and for a specific interface location ($z_i = 0.5$ m). Red dots represent the numerical solution to the problem and black solid lines predicted results calculated from equation (48).

28.5, 36.3, 42.3, 47.3, 53.3, 61.3, and 71.3 cm from the bottom of the sand column. The long electrodes crossed the entire diameter of the column such as the voltage readings represented averaged values over the cross-sectional area. The electrical conductivity was estimated from calibrated EC-voltage linear relationships obtained for each electrode by conducting a series of saline-water injection tests.

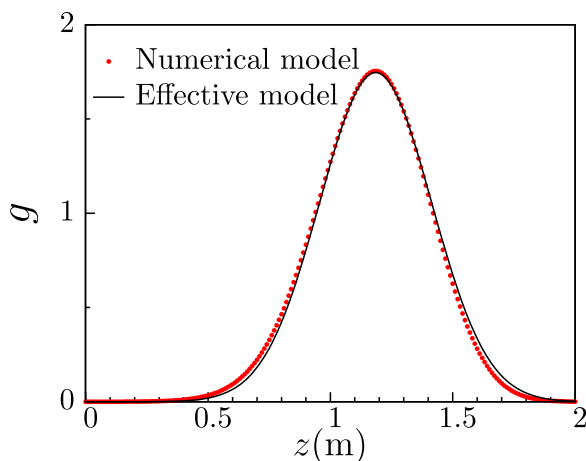


Figure 7. Gradient of the salt mass fraction distribution for $2\pi t/\tau = 33,400$, $S = 1e-1$ and $z_i = 1$ m. Red dots represent numerical results and the solid black line represents the predicted solution calculated from equation (47).

5.1. Experimental Setup

The experiments were conducted using a polycarbonate column of 15 cm in internal diameter and 90 cm in length. The filling material was medium-grained quartz sand (30-CFS grade, Sloan Sands, Dry Creek, South Australia). The sand packing was carried out by gradually adding thin sand layers which were stirred with a thin stick and compacted to avoid air entrapment. Once the column was sand-filled, the interstitial air was displaced by flushing with freshwater from the bottom up at a very low flow rate. For all the experiments, freshwater was prepared from boiled and deionized water. Uniform flow through the cross-sectional area at the bottom of the column was assured by placing a spreader and a thin nylon mesh between the column inlet/outlet and the packed bed. A glass beads layer of about 10 cm thickness was placed on the surface of the packed column to ensure fully saturated conditions in the sand and reduce capillarity effects.

The pore water pressures were monitored using eight pressure transducers (P1–P8) located at different depths (4.3, 27, 36, 43, 43, 48.5, 54, 61, and 70 cm from the bottom of the sand column). The piezometric head was calculated from the pressure readings. In order to measure the electrical conductivity (EC), eight voltage electrodes (W1–W8) were located at approximate distances of 18.2, 28.5, 36.3, 42.3, 47.3, 53.3, 61.3, and 71.3 cm from the bottom of the sand column. The long electrodes crossed the entire diameter of the column such as the voltage readings represented averaged values over the cross-sectional area. The electrical conductivity was estimated from calibrated EC-voltage linear relationships obtained for each electrode by conducting a series of saline-water injection tests.

Prior to the transient forcing test, a series of Darcy-column tests and tracer breakthrough experiments were carried out to determine the flow and transport parameters of the sand as well as the degree of heterogeneity. For these experiments, the flow rate of the injected water and tracers was controlled by a peristaltic pump (Master FLEX, L/S 7519-25) connected to the bottom of the sand column.

For the transient forcing experiment, first saline water was injected into the sand column, initially saturated with freshwater, until the interface between the two fluids was located at a distance $z_i = 0.4$ m. The sand

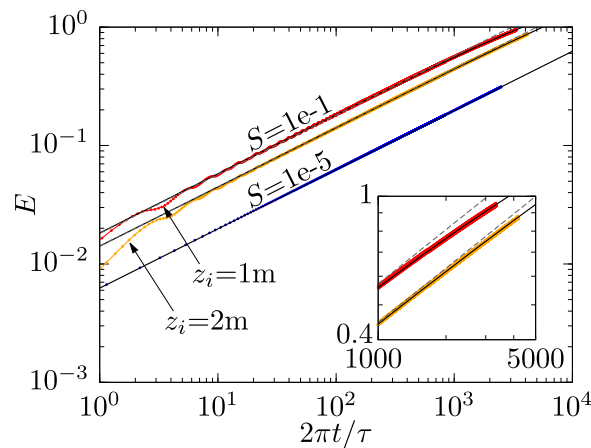


Figure 8. Temporal evolution of the dilution index. Blue dots represent numerical results for $S = 1e-5$, red and orange dots for $S = 1e-1$ with $z_i = 1\text{ m}$ and $z_i = 2\text{ m}$, respectively, black solid lines represent predictions from the equation (49) and gray dashed lines represent results for the linear regime ($E(t) \propto t^{1/2}$). The inset magnifies the subdiffusive regime of the dilution index as $E(t) \propto t^{1/4}$.

column was then connected to a saline-water reservoir column, in which a weighted piston with length 35 cm and diameter of 6.75 cm was introduced, which induced a periodic head difference between the two columns through its sinusoidal up-down displacement. The experimental setup is shown in Figure 9.

5.2. Experimental Results

The hydraulic conductivity of the sand was determined from Darcy-column experiments. For these tests, freshwater was injected from the bottom up of the sand column at a range of constant flow rates (20–40 mL/s). The head gradients at the eight pressure transducers (P1–P8) were then computed, and hydraulic conductivity estimates in the range 7–12 m/d were obtained. Similar estimates were reported by Levy and Berkowitz [2003] and Chao et al. [2000].

Continuous and pulse conservative tracer experiments were conducted to evaluate the porosity and longitudinal dispersivity of the sand. First, freshwater was injected at a flow rate of 40 mL/s from the bottom up of the column in order to stabilize the flow. Once the steady state was established, i.e., head fluctuations measured at P1–P8 were negligible, saline water was then injected with calcium chloride as a conservative tracer and a fluorescent dye (Sodium Fluorescein) to help visual inspection of the mixing zone. The injections were conducted by using a T-joint which enabled an immediate switch over between the different water reservoirs. The electrical conductivity measured at the W1–W8 electrodes (EC_i) was normalized by the

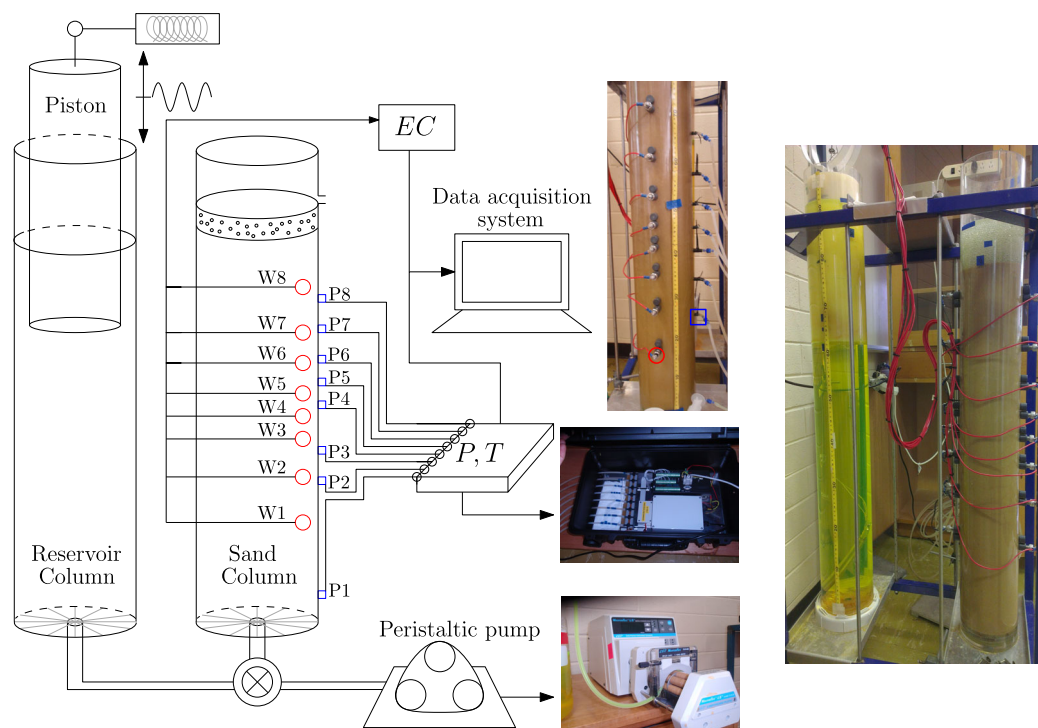


Figure 9. Schematic experimental setup of the sand column.

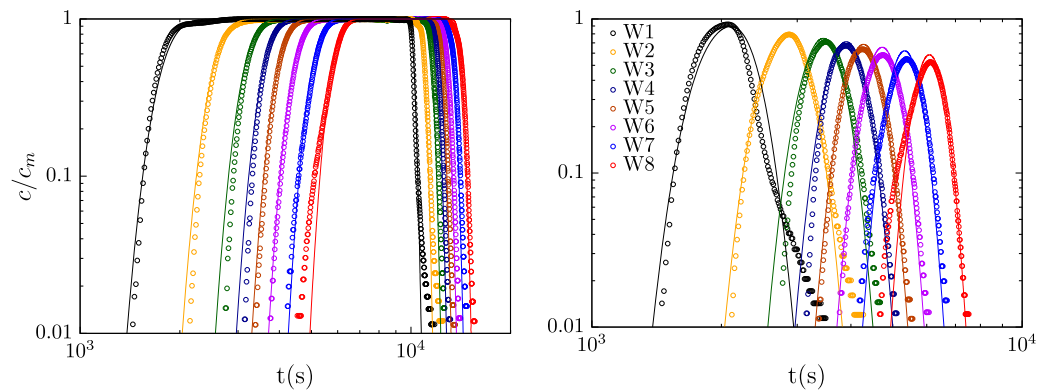


Figure 10. Breakthrough curves for the (a) continuous and (b) pulse injection tracer experiments at different depths (W1–W8). Dots represent the experimental data and solid lines the one-dimensional analytical solution.

inflow electrical conductivity (EC_m), and breakthrough curves (BTCs) were computed by assuming that the electrical conductivity is linearly related to salt mass fraction, so that $EC_i/EC_m = c_i/c_m$.

For the continuous injection test, the saline water was injected until the EC_i readings were steady and equal to the inflow EC_m at all the electrodes (2.3 h). For the pulse tracer test, the duration of the injection was about 10.6 min (1% of the characteristic advective time).

Porosity was determined from the mean arrival time of the plume center of mass ($c_i/c_m = 0.5$) for each BTC, and values in the range 0.32–0.33 were obtained. A typical range for the bulk porous matrix compressibility of sands is assumed to be between 5.2×10^{-9} to $1.4 \times 10^{-8} \text{ m}^2 \text{ kg}^{-1}$ [Domenico and Mifflin, 1965]. Considering this range and a value of 0.32 for the porosity and $4.47 \times 10^{-10} \text{ m}^2 \text{ kg}^{-1}$ for the water compressibility, specific storativity ranges between 3.5×10^{-5} to $8.6 \times 10^{-5} \text{ m}^{-1}$. Here we take the value of $5 \times 10^{-5} \text{ m}^{-1}$ for the specific storage coefficient, which corresponds to a value of $1.0 \times 10^{-8} \text{ m}^2 \text{ kg}^{-1}$ for the bulk porous matrix compressibility of the sand.

The longitudinal dispersivity was estimated by fitting the experimental BTCs to the analytical solution for the tracer injection ($t < T$) and the post freshwater injection ($t \geq T$), which reads as

$$c/c_m = \begin{cases} G(z, t) & t < T \\ G(z, t) - G(z, T) & t \geq T \end{cases} \quad (50)$$

with $G(z, t)$ the solution of the advection-dispersion equation (ADE) for a tracer injection in a one-dimensional semifinite domain [see, e.g., Ogata and Banks, 1961; Kreamer and Zuber, 1978], which is given by

$$G(z, t) = \frac{1}{2} \operatorname{erfc} \left(\frac{z-vt}{\sqrt{4D_h t}} \right) + \frac{1}{2} \exp \left(\frac{vz}{D_h} \right) \operatorname{erfc} \left(\frac{z-vt}{\sqrt{4D_h t}} \right). \quad (51)$$

A value of 0.18 cm for the longitudinal dispersivity was found to obtain an optimal fit for both the continuous and pulse tracer tests at different column depths. The comparison between the experimental BTCs and the predicted results from equation (51) is displayed in Figure 10. The results are plotted with a log-log scale to enable examination of the possible tailing behavior.

Note that the ADE model correctly predicts the Fickian behavior of the experiments and important tailing was not observed, except in the electrode W1. The observed homogeneous transport behavior of the experiment is likely caused by the uniformity of the sand, the large length of the column compared to the diameter of the grains and the long residence times [e.g., Dentz et al., 2004; Cortis et al., 2004].

For the transient forcing experiment, first freshwater was injected at a flow rate of 40 mL/s from the bottom up of the column in order to stabilize the flow. Once the steady state was reached, saline water was injected for 50 min to displace the stable density interface at a distance of $z_i = 0.4 \text{ m}$ from the bottom of the column. Once head gradients at the pressure transducers were negligible, the sand column was then connected to the saline-water reservoir column. After reaching the equilibrium between the two columns, the sinusoidal up-down displacement of the piston was activated leading to a simple harmonic forcing with an oscillation

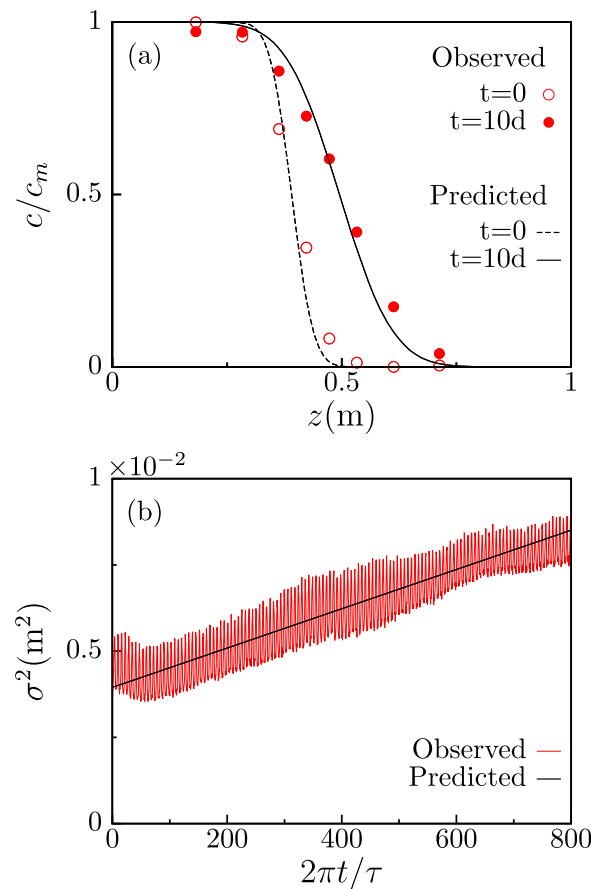


Figure 11. Experiment and predicted results of (a) the concentration distribution after the saline injection ($t = 0$) and after the influence of the temporal fluctuations of the flow conditions ($t = 10$ days) and (b) temporal evolution of the variance of the gradient of the concentration distribution from the W1–W8 electrodes (red line) and predicted results from equation (black line).

of the variance are observed. These fluctuations may be caused by the effect of small-scale heterogeneities as well as the sensitivity of the gradient calculation to the number of electrodes used.

We test the validity of the proposed effective model by comparing the model predictions with the experimental results. We first computed the concentration distribution after the initial saline injection from equation (51). From this initial gradient distribution ($t = 0$), we computed the initial value for the variance $\sigma^2(0)$ from equation (16), and its temporal evolution in response to a simple harmonic driving head from equation (42) considering a Dirichlet-type boundary condition. Finally, the concentration distribution at the end of the experiment ($t = 10$ days) was evaluated from equation (48).

The comparison of experimental and predicted results for the concentration distribution and temporal evolution of the spatial variance demonstrates that the predictions are in good agreement with the experimental results and the effective model correctly reproduces the shape of the interface and the mixing dynamics. It is important to mention that under stationary conditions ($S_s = 0$) and considering a Dirichlet-type boundary condition, there would be an instantaneous head response and $q(z, t)$ would be equal to zero (see equations (6) and (8)), obtaining a purely diffusive enhancement of the interface.

6. Conclusions

Periodic transient forcing effects lead to a spatially nonuniform time-dependent velocity field which induces enhanced spreading and mixing of solutes. We investigate dispersion and mixing of two fluids of different

amplitude of about 5 cm and period of 15,500 s. The oscillation-driven mixing experiment was run for 10 days.

In order to take into account the influence of temperature fluctuations, the EC measurements were corrected according to the equation $EC_{20} = EC_T/[1 + a(T-20)]$ [Hayashi, 2004], where EC_{20} is electrical conductivity at 20°C, EC_T is electrical conductivity measured at the electrodes at temperature T (°C) and a (°C⁻¹) is a temperature compensation factor commonly assumed to be about 2.2% [Matthess, 1982; Hem, 1985]. The gradient of concentration distribution was then computed from the corrected and normalized EC measurements.

Oscillation-driven mixing was experimentally characterized by the spatial variance (16) derived in terms of the first and second moments of the gradient of the concentration distribution computed at the electrodes. Experimental results for the concentration distribution and the spatial variance are displayed in Figure 11. Note that the interface between the two fluids was not sharp before imposing the oscillatory transient-forcing ($t = 0$), and then the spatial variance was not zero. This is due to dispersion mechanisms induced by the initial saline injection.

Experimental results show that, as expected, once the steady oscillatory state is reached (approximately 1 day), the variance increases linearly with time. Note that significant fluctuations about the mean temporal evolution

density under oscillatory transient flow. Between the two fluids a diffuse interface develops, the mixing zone, which is characterized by the spatial moments of the gradient of the solute concentration distribution and quantified by the evolution of the variance of the gradient distribution. The behavior of the mixing zone is investigated by detailed numerical simulations and column experiments. The observed behaviors are quantified by an effective model that is obtained from the time-average of the full flow and transport equations.

In the present study, two different time-fluctuating boundary conditions have been considered: a dynamic specified flux (Neumann-type), and a periodic prescribed head boundary condition (Dirichlet-type). We demonstrate that the key parameters controlling the impact of temporal fluctuations on mixing are the interface location (z_i) and the wave number ($\mu = \sqrt{S_s \pi / k \tau}$), which depends on the period and the hydraulic diffusivity. We find that fluctuation-driven mixing increases if the interface is close to the boundary, and the enhancement of the interface becomes purely diffusive for $z_i = 4.5 / \mu$. We also find that the impact of the wave number on transient-induced mixing strongly depends on the boundary conditions. Thus, for the case of using a Neumann-type boundary condition, large wave number (large storativity or short period), tends to favor the exponential decay in flow velocities with distance causing the effect of oscillatory-transient forcing on mixing to reduce [Goode and Konikow, 1990]. On the other hand, for the case of using a Dirichlet-type boundary condition, large wave number implies not only a delayed head response to temporal fluctuation, but also higher flow velocities, which leads to enhanced dispersion.

We derived an effective time-average formulation to describe the coupling between mixing and oscillatory transient flow under nonstationary flow conditions. Explicit expressions for the concentration distribution and the variance are developed to predict the transient mixing dynamics. Two dominant regimes are identified in the temporal evolution of the variance in response to the spatial and temporal variability of the velocity field induced by temporal fluctuations. At small times, the width of the mixing zone is mainly influenced by the flow velocity at the interface location and both the center of mass as well as the variance increase linearly with time. In this regime, the mixing zone dynamics can be characterized by a constant in time effective dispersion coefficient, which decreases exponentially as the initial interface location increases. For increasing times, as soon as the interface start experiences the nonlinear spatial velocity profile, the center of mass position decelerates, which leads to a compression of the interface. This deceleration results in a logarithmic upward displacement of the center of mass and a growth of the variance with $t^{1/2}$.

This study has only examined the effect of temporally fluctuating one-dimensional flow on mixing. Further analysis extending the problem to two and three dimensions and considering other physical factors such as fluid density differences and heterogeneity effects is required. Furthermore, temporal flow fluctuations usually have multiple harmonic constituent signals on multiple time scales (recharge, pumping, and tides), such that their response on the flow field may lead to more complex flow and transport dynamics. Therefore, the impact of the coupling between aquifer storativity, heterogeneity, density effects, and multiple scales of transient forcing on solute transport is required to explore the implications of these findings for the understanding of mixing and reaction processes in real systems.

Appendix A: Two-Scale Expansion of the Transport Equation

Here we derive a transport equation for the temporally averaged gradient. To this end, we first nondimensionalize the original transport equation for the gradient according to

$$z = z' \mu^{-1}, \quad t = t' \tau', \quad \alpha_L = \alpha'_L \mu^{-1}, \quad D'_m = \mu^2 \tau D_m, \tag{A1}$$

with the period $\tau' = \tau / (2\pi)$.

The dimensionless pore water velocity reads as

$$v'(z', t') = \mu \tau' v_0 \exp(-z') \sin(t' - z' + \varphi). \tag{A2}$$

where for the Neumann boundary conditions we define

$$v_0 = \frac{Ak}{\phi L}, \quad \varphi = 0, \tag{A3}$$

while for the Dirichlet boundary conditions, we define

$$v_0 = \sqrt{2} \frac{Ak\mu}{\phi}, \quad \phi = \frac{\pi}{4}. \tag{A4}$$

Thus, equation (13) for the gradient reads as

$$\frac{\partial g(z', t')}{\partial t'} + \frac{\partial}{\partial z'} v'(z', t') g(z', t') - \frac{\partial^2}{\partial z'^2} [\alpha'_L |v'(z', t') + D'_m] g(z', t') = 0. \tag{A5}$$

We seek the behavior on time scales $T \gg \tau'$. The latter provides the small expansion parameter $\epsilon = \tau'/T \ll 1$. Thus, we now define the "slow" time $t_s = \epsilon^2 t'$ and write

$$g(z', t') = \hat{g}(z', \epsilon^2 t', t'). \tag{A6}$$

This gives for (A5)

$$\begin{aligned} \epsilon^2 \frac{\partial \hat{g}(z', t_s, t')}{\partial t_s} + \frac{\partial \hat{g}(z', t_s, t')}{\partial t'} + \frac{\partial}{\partial z'} v'(z', t') \hat{g}(z', t_s, t') \\ - \frac{\partial^2}{\partial z'^2} [\alpha'_L |v'(z', t') + D'_m] \hat{g}(z', t_s, t') = 0. \end{aligned} \tag{A7}$$

We now assume that $\hat{g}(z, t_s, t')$ can be expanded in ϵ as

$$\hat{g}(z, t_s, t') = \hat{g}_0(z, t_s, t') + \sum_{i=1}^{\infty} \hat{g}_i(z, t_s, t'), \tag{A8}$$

where the $\hat{g}_i(z', t_s, t')$ are of order ϵ^i . Note that $v'(z', t')$ is of order ϵ and further assume that α'_L is of order ϵ as well. We furthermore require $\hat{g}_i(z', t_s, t')$ to be periodic in t' . Inserting this expansion into (A7) we obtain at order ϵ^0

$$\frac{\partial \hat{g}_0(z', t_s, t')}{\partial t'} = 0, \tag{A9}$$

from which follows that $\hat{g}_0(z', t_s, t') \equiv \hat{g}_0(z', t_s)$. At order ϵ , we have

$$\frac{\partial \hat{g}_1(z', t_s, t')}{\partial t'} = - \frac{\partial}{\partial z'} v'(z', t') \hat{g}_0(z', t_s). \tag{A10}$$

At order ϵ^2 , we obtain the equation

$$\begin{aligned} \epsilon^2 \frac{\partial \hat{g}_0(z', t_s)}{\partial t_s} + \frac{\partial \hat{g}_2(z', t_s, t')}{\partial t'} + \frac{\partial}{\partial z'} v'(z', t') \hat{g}_1(z', t_s, t') \\ - \frac{\partial^2}{\partial z'^2} [\alpha'_L |v'(z', t') + D'_m] \hat{g}_0(z', t_s) = 0 \end{aligned} \tag{A11}$$

Averaging over a period gives the governing equation for $\hat{g}_0(z', t_s)$ as

$$\epsilon^2 \frac{\partial \hat{g}_0(z', t_s)}{\partial t_s} + \frac{\partial}{\partial z'} \overline{v'(z', t') \hat{g}_1(z', t_s, t')} - \frac{\partial^2}{\partial z'^2} [\hat{D}_e(z') + D'_m] \hat{g}_0(z', t_s) = 0, \tag{A12}$$

where we used that $\hat{g}_2(z', t_s, t')$ is periodic in t' . The overbar denotes the temporal averaging over a period. We furthermore defined the effective dispersion coefficient

$$\hat{D}_e(z') = \frac{1}{2\pi} \int_0^{2\pi} dt' \alpha'_L |v'(z', t')|. \tag{A13}$$

Using the dimensionless velocity (A2) gives

$$\hat{D}_e(z) = \frac{2\alpha'_L \mu \tau' v_0}{\pi} \exp(-z'). \tag{A14}$$

In order to determine the average in second term in (A12), we first derive the expression for $\hat{g}_1(z', t_s, t')$. We obtain from (A10) by using (A2) the following expression:

$$\hat{g}_1(z', t_s, t') = v_0 \mu \tau' \exp(-z') \left[\sin(t' - z') \hat{g}_0(z', t_s) - \cos(t' - z') \frac{\partial \hat{g}_0(z', t_s)}{\partial z'} \right]. \quad (A15)$$

Multiplying the latter with (A2) gives

$$v'(z', t') \hat{g}_1(z', t_s, t') = (v_0 \mu \tau')^2 \exp(-2z') \left[\sin(t' - z')^2 \hat{g}_0(z', t_s) - \sin(t' - z') \cos(t' - z') \frac{\partial \hat{g}_0(z', t_s)}{\partial z'} \right]. \quad (A16)$$

Averaging over the period of 2π gives

$$\overline{v'(z', t') \hat{g}_1(z', t_s, t')} = \frac{(v_0 \mu \tau')^2 \exp(-2z')}{2} \hat{g}_0(z', t_s). \quad (A17)$$

Thus, we obtain for $g_0(z', t)$ the governing equation

$$\epsilon^2 \frac{\partial \hat{g}_0(z', t_s)}{\partial t_s} + \frac{\partial}{\partial z'} \hat{v}_e(z') \hat{g}_1(z', t_s, t') - \frac{\partial^2}{\partial z'^2} [\hat{D}_e(z') + D'_m] \hat{g}_0(z', t_s) = 0. \quad (A18)$$

We obtain (23) by casting (A12) in dimensional terms using $t_s = \epsilon^2 t'$ and (A1).

Appendix B: Approximate Solution for the Variance

Using (24) and (30), we obtain for $\gamma(t)$ and $\mathcal{D}(t)$ defined in (36) the explicit expressions

$$\gamma(t) = \frac{v_0^2 \mu^2 \tau \exp(-2\mu z_i)}{2\pi} \left[\frac{v_0^2 \mu^2 \tau \exp(-2\mu z_i) t}{2\pi} + 1 \right]^{-1}, \quad (B1)$$

$$\mathcal{D}(t) = \frac{2\alpha_L v_0 \exp(-\mu z_i)}{\pi} \left[\frac{v_0^2 \mu^2 \tau \exp(-2\mu z_i) t}{2\pi} + 1 \right]^{-1/2}. \quad (B2)$$

Thus, we obtain for $\Gamma(t)$ defined in (41)

$$\Gamma(t) = \ln \left[\frac{v_0^2 \mu^2 \tau \exp(-2\mu z_i) t}{2\pi} + 1 \right]. \quad (B3)$$

Inserting these expressions into (40) gives

$$\begin{aligned} \sigma^2(t) = & \frac{\sigma^2(0)}{\left[\frac{v_0^2 \mu^2 \tau \exp(-2\mu z_i) t}{2\pi} + 1 \right]^2} + \frac{2}{\left[\frac{v_0^2 \mu^2 \tau \exp(-2\mu z_i) t}{2\pi} + 1 \right]^2} \times \\ & \int_0^t dt' \left(\frac{2\alpha_L v_0 \exp(-\mu z_i)}{\pi} \left[\frac{v_0^2 \mu^2 \tau \exp(-2\mu z_i) t'}{2\pi} + 1 \right]^{-1/2} + D_m \right) \times \\ & \left[\frac{v_0^2 \mu^2 \tau \exp(-2\mu z_i) t'}{2\pi} + 1 \right]^2. \end{aligned} \quad (B4)$$

Carrying out the integration and after rearrangement of terms gives the analytical expression (42) for the variance.

Acknowledgments

The data used in this paper can be obtained upon request from the corresponding author. The support of the European Research Council (ERC) through the project MHetScale (617511) is gratefully acknowledged. We also wish to thank the assistance provided by Flinders University mechanical workshop staff, in particular Andrew Dunn and Christopher Price.

References

- Abarca, E., E. Vazquez-Sune, J. Carrera, B. Capino, D. Gamez, and F. Batlle (2006), Optimal design of measures to correct seawater intrusion, *Water Resour. Res.*, *42*, W09415, doi:10.1029/2005WR004524.
- Attinger, S., M. Dentz, H. Kinzelbach, and W. Kinzelbach (1999), Temporal behavior of a solute cloud in a chemically heterogeneous porous medium, *J. Fluid Mech.*, *386*, 77–104.
- Bear, J. (1972), *Dynamics of Fluids in Porous Media*, 764 pp., Elsevier, Amsterdam, Netherlands.
- Bonnesen, E. P., F. Larsen, T. O. Sonnenborg, K. Klitten, and L. Stemmerik (2009), Deep saltwater in chalk of north-west Europe: Origin, interface characteristics and development over geological time, *Hydrogeol. J.*, *17*(7), 1643–1663, doi:10.1007/s10040-009-0456-9.
- Chao, H.-C., H. Rajaram, and T. Illangasekare (2000), Intermediate-scale experiments and numerical simulations of transport under radial flow in a two-dimensional heterogeneous porous medium, *Water Resour. Res.*, *36*(10), 2869–2884.

- Chen, H., and G. F. Pinder (2011a), Investigation of groundwater contaminant discharge into tidally influenced surface-water bodies: Experimental results, *Transp. Porous Media*, 89(3), 307–321, doi:10.1007/s11242-011-9771-4.
- Chen, H., and G. F. Pinder (2011b), Investigation of groundwater contaminant discharge into tidally influenced surface-water bodies: Theoretical analysis, *Transp. Porous Media*, 89(3), 289–306, doi:10.1007/s11242-011-9772-3.
- Cirpka, O. A., and S. Attinger (2003), Effective dispersion in heterogeneous media under random transient flow conditions, *Water Resour. Res.*, 39(9), 1257, doi:10.1029/2002WR001931.
- Cortis, A., Y. Chen, H. Scher, and B. Berkowitz (2004), Quantitative characterization of pore-scale disorder effects on transport in homogeneous granular media, *Phys. Rev. E*, 70(4), 041178, doi:10.1103/physreve.70.041108.
- Dagan, G., A. Bellin, and Y. Rubin (1996), Lagrangian analysis of transport in heterogeneous formations under transient flow conditions, *Water Resour. Res.*, 32(4), 891–899, doi:10.1029/95WR02497.
- de Dreuzy, J.-R., J. Carrera, M. Dentz, and T. Le Borgne (2012), Asymptotic dispersion for two-dimensional highly heterogeneous permeability fields under temporally fluctuating flow, *Water Resour. Res.*, 48, W01532, doi:10.1029/2011WR011129.
- Dentz, M., and J. Carrera (2003), Effective dispersion in temporally fluctuating flow through a heterogeneous medium, *Phys. Rev. E*, 68(3), 036310.
- Dentz, M., and F. P. J. de Barros (2015), Mixing-scale dependent dispersion for transport in heterogeneous flows, *J. Fluid Mech.*, 777, 178–195, doi:10.1017/jfm.2015.351.
- Dentz, M., H. Kinzelbach, S. Attinger, and W. Kinzelbach (2000), Temporal behavior of a solute cloud in a heterogeneous porous medium: 1. Point-like injection, *Water Resour. Res.*, 36(12), 3591–3604.
- Dentz, M., A. Cortis, H. Scher, and B. Berkowitz (2004), Time behavior of solute transport in heterogeneous media: Transition from anomalous to normal transport, *Adv. Water Resour.*, 27(2), 155–173.
- Dentz, M., J. Carrera, and J. R. De Dreuzy (2011a), Erratum: Effective dispersion in temporally fluctuating flow through a heterogeneous medium [phys. rev. e 68, 036310 (2003)], *Phys. Rev. E*, 84, 019904(E).
- Dentz, M., T. Le Borgne, A. Englert, and B. Bijeljic (2011b), Mixing, spreading and reaction in heterogeneous media: A brief review, *J. Contam. Hydrol.*, 120, 1–17.
- Domenico, P. A., and M. D. Mifflin (1965), Water from low-permeability sediments and land subsidence, *Water Resour. Res.*, 1(4), 563–576, doi:10.1029/wr001i004p00563.
- Ferris, J. (1951), Cyclic fluctuations of water level as a basis for determining aquifer transmissibility, *Int. Assoc. Sci. Hydrol.*, 33, 148–155.
- Freeze, R. A., and J. A. Cherry (1979), *Groundwater*, 604 pp., Prentice-Hall, Englewood Cliffs, N. J.
- Frind, E. (1982), Simulation of long-term transient density-dependent transport in groundwater, *Adv. Water Resour.*, 5, 73–88.
- Goode, D. J., and L. Konikow (1990), Apparent dispersion in transient groundwater flow, *Water Resour. Res.*, 26(10), 2339–2351.
- Hayashi, M. (2004), Temperature-electrical conductivity relation of water for environmental monitoring and geophysical data inversion, *Environ. Monit. Assess.*, 96(1–3), 119–128, doi:10.1023/b:emas.0000031719.83065.68.
- Hem, J. D. (1985), Study and interpretation of the chemical characteristics of natural water, *U.S. Geol. Surv. Water Supply Pap.*, 2254, pp. 67.
- Jacob, C. E. (1950), Flow of groundwater, in *Engineering Hydraulics*, edited by H. Rouse, pp. 321–386, John Wiley, N. Y.
- Kinzelbach, W. (1988), The random-walk method in pollutant transport simulation, *NATO ASI Ser. C*, 224, 227–246.
- Kinzelbach, W., and P. Ackerer (1986), Modélisation de la propagation d'un contaminant dans un champ d'écoulement transitoire, *Hydro-geologie*, 2, 197–206.
- Kitanidis, P. (1988), Prediction by the method of moments of transport in a heterogeneous formation, *J. Hydrol.*, 102(1–4), 453–473.
- Kitanidis, P. K. (1994), The concept of the dilution index, *Water Resour. Res.*, 30(7), 2011–2026, doi:10.1029/94WR00762.
- Kreft, A., and A. Zuber (1978), On the physical meaning of the dispersion equation and its solutions for different initial and boundary conditions, *Chem. Eng. Sci.*, 33(11), 1471–1480, doi:10.1016/0009-2509(78)85196-3.
- Le Borgne, T., M. Dentz, and E. Villermaux (2013), Stretching, coalescence, and mixing in porous media, *Phys. Rev. Lett.*, 110(20), 204501.
- Levy, M., and B. Berkowitz (2003), Measurement and analysis of non-Fickian dispersion in heterogeneous porous media, *J. Contam. Hydrol.*, 64(3–4), 203–226, doi:10.1016/s0169-7722(02)00204-8.
- Matthess, G. (1982), *The Properties of Groundwater*, John Wiley, N. Y.
- Medina, A., and J. Carrera (2003), Geostatistical inversion of coupled problems: Dealing with computational burden and different types of data, *J. Hydrol.*, 281(4), 251–264.
- Ogata, A., and R. B. Banks (1961), A solution of the differential equation of longitudinal dispersion in porous media, *U.S. Geol. Surv. Prof. Pap.*, 411-A.
- Oki, D. S., W. R. Souza, E. L. Bolke, and G. R. Bauer (1998), Numerical analysis of the hydrogeologic controls in a layered coastal aquifer system, Oahu, Hawaii, USA, *Hydrogeol. J.*, 6(2), 243–263, doi:10.1007/s100400050149.
- Rajaram, H., and L. Gelhar (1993), Plume scale-dependent dispersion in heterogeneous aquifers: 1. Lagrangian analysis in a stratified aquifer, *Water Resour. Res.*, 29(9), 3249–3260.
- Rehfeldt, K., and L. Gelhar (1992), Stochastic analysis of dispersion in unsteady flow in heterogeneous aquifers, *Water Resour. Res.*, 28, 2085–2099.
- Risken, H. (1996), *The Fokker-Planck Equation*, Springer, N. Y.
- Stoessell, R. K. (1995), Dampening of transverse dispersion in the halocline in karst limestone in the northeastern Yucatan peninsula, *Groundwater*, 33(3), 366–371, doi:10.1111/j.1745-6584.1995.tb00291.x.
- Townley, L. R. (1995), The response of aquifers to periodic forcing, *Adv. Water Resour.*, 18(3), 125–146, doi:10.1016/0309-1708(95)00008-7.
- Van Der Kamp, G. (1972), Tidal fluctuations in a confined aquifer extending under the sea, *Proceedings of International Geological Congress*, 24(1), 101–106.
- Vázquez-Suñé, E., J. Carrera, E. Abarca, and B. Capino (2005), Estimation of recharge floods in disconnected stream-aquifers systems. Application to the Baix Llobregat aquifers, Barcelona, Spain, *J. Hydrol.*, 45, 579–589.
- Voss, C. I., and W. R. Souza (1987), Variable density flow and transport simulation of regional aquifers containing a narrow freshwater-saltwater transition zone, *Water Resour. Res.*, 23(10), 1851–1866.